Journal of Energy Storage 97 (2024) 112683

Contents lists available at ScienceDirect

Journal of Energy Storage

journal homepage: www.elsevier.com/locate/est

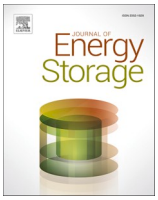

Research papers

Symmetric double-layer capacitor with natural rubber and sodium salt-based solid polymer electrolyte and reduced graphene oxide electrodes

Kumudu S. Perera [a,*], Kamal P. Vidanapathirana [a], Lewis J. Adams [b], Chris S. Hawes [b], Nilanthy Balakrishnan [b,*]

[a] Department of Electronics, Faculty of Applied Sciences, Wayamba University of Sri Lanka, Kuliyapitiya 60200, Sri Lanka
[b] School of Chemical and Physical Sciences, Keele University, Keele ST5 5BG, UK

ARTICLE INFO

Keywords:
Reduced graphene oxide
Natural rubber
Sodium trifluoromethanesulfonate
Solid polymer electrolyte
Double-layer capacitor

ABSTRACT

Solid polymer electrolytes (SPEs) are the key to improving electrochemical devices' energy density and safety. In recent years, natural polymers have received tremendous attention due to the latest advances in green technology for a sustainable future. Herein, SPEs based on 49 % methyl grafted natural rubber (MG49-NR) and sodium trifluoromethanesulfonate ($Na(CF_3SO_3)$ – NaTF) salt were prepared and characterized to optimize their performance. The composition MG49-NR: NaTF = 1:0.5 (by weight) shows the highest room temperature conductivity (σ_{RT}) of 7.52×10^{-4} S cm^{-1}. This optimized electrolyte is purely an ionic conductor with an activation energy (E_a) of 0.29 eV. The optimized electrolyte was used to fabricate double-layer capacitors by sandwiching it between two identical reduced graphene oxide (rGO) electrodes. The fabricated double-layer capacitors show a maximum single electrode specific capacitance (C_{sc}) of 42.5 F g^{-1} from the cyclic voltammetry (CV) test. Moreover, the charge storage mechanism utterly takes place via non-faradaic reactions which is evidenced by cyclic voltammograms. Furthermore, the electrochemical impedance spectroscopy (EIS) test shows the capacitive features are dominant at low frequencies. Performance of the double-layer capacitor during 10,000 charge and discharge cycles at a constant current density of 0.05 A g^{-1} shows a fast drop of single electrode specific discharge capacitance (C_{sd}) at the beginning, but it started to saturate after the 5000th cycle proving the good stability of the capacitor. These findings are relevant to expanding the functionalities of SPE-based double-layer capacitors in green technologies.

1. Introduction

In the current era, there is a clear awareness of environmental issues such as global warming, climate change, ozone layer depletion, acid rain and forest fires. Therefore, scientists have been continuously working to find solutions to create a sustainable future. The latest innovations in green technology can help industries to find alternative and sustainable ways of using more natural materials for cheap, safe, and eco-friendly products [1]. Several green technologies attempt to reduce climate change by minimizing carbon dioxide and other greenhouse gas emissions. In addition, renewable energy sources like solar and wind could be the ultimate solution for the substitute for fossil fuel. Moreover, to ease the gap between the energy supply and demand on the grid, sustainable energy storage devices are needed. This increased the research interest in electrochemical energy storage devices, such as batteries, supercapacitors, and fuel cells. Fuel cells and batteries offer higher energy densities ($\geq 10^2$ Wh kg^{-1}) while supercapacitors offer an excellent power-to-weight ratio which makes them suitable for high power

Abbreviations: SPE, Solid polymer electrolyte; NR, Natural rubber; MG-NR, methyl grafted; PMMA, poly(methyl methacrylate); MG49-NR, 49 % poly(methyl methacrylate) grafted natural rubber; NaTF, Sodium trifluoromethanesulfonate ($Na(CF_3SO_3)$); rGO, Reduced graphene oxide; AC, Activated carbon; THF, Tetrahydrofuran; NMP, *N*-methyl-2-pyrrolidone; PVdF, polyvinylidene fluoride; EDLC, electric double-layer capacitor; SS, Stainless steel; σ, Conductivity; σ_{RT}, Room temperature conductivity; E_a, Activation energy; τ_0, Relaxation time constant; C_{sc}, Specific capacitance; C_{sd}, Specific discharge capacitance; EIS, Electrochemical impedance spectroscopy; BET, Brunauer-Emmett-Teller; QSDFT, Quenched Solid Density Functional Theory; GCD, Galvanostatic charge discharge; CV, Cyclic voltammetry; XRD, X-ray diffraction; ATR-FTIR, Attenuated total reflection Fourier transform infrared; SEM, Scanning electron microscopy; EDX, Energy dispersive X-ray; DC, Direct current.

* Corresponding authors.
E-mail addresses: kumudu@wyb.ac.lk (K.S. Perera), n.balakrishnan@keele.ac.uk (N. Balakrishnan).

https://doi.org/10.1016/j.est.2024.112683
Received 16 January 2024; Received in revised form 9 June 2024; Accepted 16 June 2024

requirements released in a short period [2]. Over recent years, there has been a growing demand for supercapacitors due to modern applications like electric vehicles and power back-ups that require fast charge release.

In general, supercapacitors consist of an electrolyte sandwiched between two electrodes. After the trailblazing work of Wright's group in 1973, solid polymer electrolytes (SPEs) received tremendous attention as a viable substitute for liquid electrolytes because liquid electrolytes have various demerits such as leakage, evaporation, and limited design flexibility [3]. As a result, SPEs have been extensively used for a broad range of electrochemical applications including electrochromic displays, sensors, supercapacitors, and rechargeable batteries [4,5]. Typically, a SPE contains a polymer, a salt, and solvent(s). So far, a great amount of work has been done by researchers from all around the globe aiming to improve the properties of SPEs. With the initiation and popularization of the concepts related to green technology, much attention has been focused on searching for safe and environmentally friendly polymers and salts to get rid of toxic solvents.

Traditionally, natural rubber (NR) is considered as a good insulator. However, the rapid progress of science and technology has been able to prove the suitability of NR to be used for SPEs upon tuning its properties via chemical modifications [6]. NR receives an oxygen atom with one pair of electrons that forms a coordination bond with cation from metal salts leading to form polymer-salt complexes. The modified NR exhibits soft elastomer features [7]. In addition, its elasticity properties are expected to improve upon modification and that gives rise to satisfactory contacts between the electrode and the electrolyte. Their low glass transition temperatures favour a more amorphous phase for segmental motion which is a key attribute to gain higher preference from the point of view of applications. From the modified NR types, epoxidized and methyl grafted NR (MG-NR) groups have received notable attention. However, epoxidized NR has faced some challenges in use for applications due to its stickiness and difficulty in peeling from substrates [8]. Hence, MG-NR has attracted the interest of many researchers to prepare SPEs. However, the investigation focus has been mostly towards rechargeable cells [6]. Typically, MG-NR is labelled with the number of methyl groups grafted like MG30-NR, and MG49-NR. MG49-NR has received more attention as it has the highest number of methyl groups (49 %) grafted to the NR backbone.

Many research studies have been done on different cell configurations with MG49-NR + Li salt-based electrolytes due to the attractive performance of Li systems [9–11]. However, to reduce the reliance on Li resources and for the advancement of long-term sustainable energy storage technology, we have selected the Na-based salt of sodium trifluoromethanesulfonate (Na(CF3SO3) –NaTF) for this study. Na is an abundant resource which is more user and environmentally friendly than Li. Also, Na-based salts are available at a lower cost than Li-based salts. Only a few research groups including us have fabricated and reported electric double-layer capacitors (EDLCs) using diverse electrolytes based on MG49-NR [12–14]. Recently, we reported an EDLC with a Zn salt-based MG49-NR electrolyte [15]. Compared to Zn, Na salt is expected to demonstrate higher performance due to its monovalent nature and smaller size.

In this study, we optimized the composition of MG49-NR and NaTF salt-based SPEs to get the maximum room temperature ionic conductivity. The electrolytes were characterized by X-ray diffraction (XRD) and attenuated total reflection Fourier transform infrared (ATR-FTIR) spectroscopy to understand the relation between the conductivity and structural changes in the polymer-salt matrix. Moreover, the optimized electrolyte was characterized by scanning electron microscopy (SEM) and energy dispersive X-ray (EDX) spectroscopy to study its morphology. Then, we fabricated and characterized double-layer capacitors using rGO electrodes. rGO has higher electrical conductivity and specific surface area than its parental material of natural graphite which favours higher capacitive properties. According to our knowledge, this is the first investigation for a double-layer capacitor with MG49-NR + Na salt-based electrolyte and rGO electrodes.

2. Experimental section

2.1. Preparation and characterization of electrolyte

MG49-NR (purity 99 %) was obtained from Associated Speciality Rubbers from Sri Lanka. The NaTF salt (purity 98 %, MW 172.06) and tetrahydrofuran (THF) (purity 99.9 %, MW 72.11) were purchased from Sigma Aldrich. The electrolyte preparation method can influence the device's performance. The solvent casting method that used to prepare the electrolyte is very sensible to atmospheric conditions, such as humidity and temperature. Under high humidity, it takes more time to evaporate the solvent, THF. Hence, it is important to perform the solvent evaporation of electrolytes in a controlled atmosphere. Moreover, appropriate mixing of MG49-NR and the salt is highly essential for obtaining a homogeneous film at the end. This can be assured via a long-time magnetic stirring. Fig. 1 illustrates the electrolyte preparation steps. Firstly, MG49-NR was minced, and the required weight was dissolved in THF for 12 h. Secondly, continuous magnetic stirring was done for 24 h. Also, the required weight of NaTF salt was separately dissolved in THF via magnetic stirring for 24 h. Then, both solutions were mixed, and magnetic stirring was continued for another 24 h. A homogeneous, clear solution was obtained, and it was poured into a glass petri dish and left to evaporate the THF leading to thin film formation. The formation of a clear film is evidence for the complete evaporation of THF. Several samples were prepared using different salt ratios (MG49-NR: NaTF = 1:x, by weight). The thickness of each electrolyte is around 0.3 mm.

The prepared electrolyte samples were characterized by the surface-sensitive ATR-FTIR spectroscopy using the Nicolet iS10 FTIR spectrometer equipped with a standard KBr beam splitter and DTGS detector over a wavenumber range of 4000 to 650 cm^{-1} with a scanning step of 0.24 cm^{-1}. The reference samples MG49-NR polymer and NaTF salt were also characterized by ATR-FTIR. The XRD data were collected with a D8 Advanced powder diffractometer using a monochromatic Cu-Kα radiation source of wavelength $\lambda_\alpha = 1.5418$ Å and an LYNXEYE XE (1D mode) detector for a 2θ range of 5° to 50°.

A circular-shaped sample from each electrolyte prepared with different salt concentrations was loaded in between two stainless steel (SS) electrodes in a sample holder. Electrochemical Impedance Spectroscopy (EIS) data were collected within the frequency range of 2 MHz to 200 Hz at room temperature ($T = 300$ K) using a computer-controlled impedance analyser (IVUM Stat). The thickness of each sample was measured with a micrometre screw gauge. Upon analysing impedance data, conductivity, σ of each sample was calculated using Eq. (1),

$$\sigma = \left(\frac{1}{R_b}\right)\left(\frac{t}{A}\right) \tag{1}$$

where R_b, t, A are the bulk electrolyte resistance, thickness, and area of the electrolyte, respectively [9]. The sample that showed the highest room temperature conductivity was selected for further studies, including SEM imaging and EDX spectroscopy for morphological analysis using the Hitachi S4500 Microscope at acceleration voltages 10 kV and 15 kV, respectively. For the highest conductive sample, impedance data were gathered within the frequency range of 2 MHz to 200 Hz by varying the temperature from room temperature to 50 °C using a Buchi-type glass tube furnace. Impedance data were measured at different temperatures to find the relationship between the conductivity and the temperature. Another circular-shaped sample from the same electrolyte composition was loaded in between two SS electrodes in a sample holder as before. By applying a direct current (DC) bias potential of 500 mV, the current variation across the sample was measured at different time intervals. Current variation with time was plotted to calculate the contribution of ions and electrons for the conductivity.

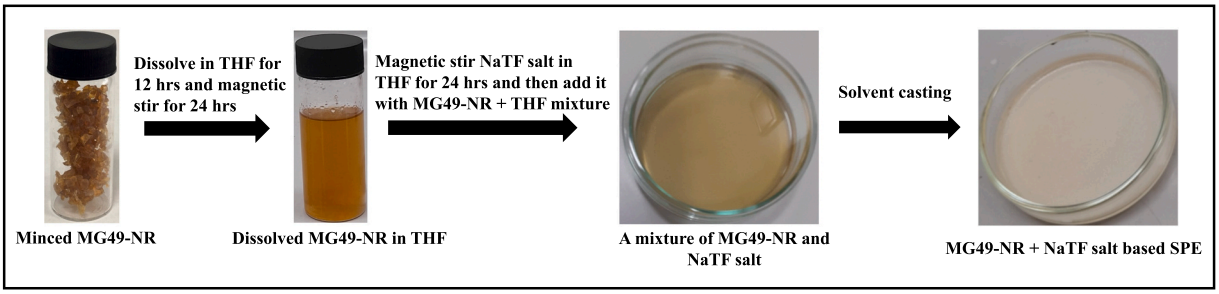

Fig. 1. Preparation steps of MG49-NR + NaTF salt solid polymer electrolyte.

2.2. Preparation and characterization of electrodes

To prepare high-quality electrodes, we have adopted the doctor blade method used for dye-sensitized solar cell fabrication [16]. rGO was received from Sakura Graphite, Ragedara Mine, Sri Lanka and used without any prior treatment. Activated carbon (AC) (MW 12.01), polyvinylidene fluoride (PVdF) (purity 99.5 %, MW 64.03), *N*-methyl-2-pyrrolidone (NMP) (MW 99.13) and fluorine-doped tin oxide (FTO) glass were purchased from Sigma Aldrich. rGO was mixed with AC and PVdF in the mass ratio of 80:10:10, respectively using NMP as the solvent. A thick slurry was obtained by grinding the mixture using a mortar and a pestle. The resultant slurry was applied on FTO glass plates having a surface area of 1 cm^2. The rGO-coated FTO plates were then dried at 50 °C for 2 h. The selected mass loading was 4 mg cm^{-2}. The rGO-based electrode with the highest single electrode specific capacitance (C_{sc}) was characterized by SEM using the Hitachi S4500 Microscope at an acceleration voltage of 10 kV.

The Brunauer-Emmett-Teller (BET) surface area analysis was performed on the pristine rGO and the rGO composite (rGO: AC: PVdF = 80:10:10) to study their porous size distribution. All adsorption measurements were performed using a Quantachrome Autosorb iQ with N4.5 grade N_2 and He gases. Both samples were pre-activated prior to measurement by heating at 100 °C for 6 h under a high vacuum provided by an Edwards rotary vacuum pump, followed by further activation at 100 °C on the instrument outgasser station with a high vacuum ($\sim 10^{-9}$ mbar) provided by a turbomolecular pump. Instrument control and data reduction were controlled using Quantachrome ASiQwin version 5.21. BET surface areas were calculated based on adsorption points chosen from the Rouquerol criteria. Pore size distribution was calculated using a Quenched Solid Density Functional Theory (QSDFT) equilibrium model assuming slit-shaped pores on a carbon adsorbent. The BET fitting parameters are provided in Table S1.

2.3. Fabrication and characterization of double-layer capacitors

The optimized electrolyte film was sandwiched between two identical rGO-based electrodes and sealed. For EIS measurements, the double-layer capacitor was connected to a computer-controlled impedance analyser (IVUM Stat). Under the effect of a small amplitude alternating current signal, impedance data were taken within the frequency range of 400 kHz to 0.001 Hz at room temperature. Cyclic voltammetry (CV) test was done using a three-electrode setup. One electrode of the double-layer capacitor was used as the working electrode while the others were used as reference and counter electrodes. Variation of current was measured within different potential windows and at different scan rates. Then, the stability of the capacitor to withstand continuous operation was monitored by cycling 500 times. The galvanostatic charge discharge (GCD) test was performed for 10,000 cycles under a constant current density of 0.05 A g^{-1} within the potential window of 0.2 V to 1.2 V.

3. Results and discussion

3.1. Optimization of solid polymer electrolyte

The ionic conductivity, σ is an important parameter of an electrolyte for its applications. One method of optimizing σ is engineering the material composition of the electrolyte. In this work, NaTF concentration was varied keeping the MG49-NR concentration at a constant value of 1. Variation of NaTF concentration was done as $1 : x$ (by weight) where x represents the ratio of NaTF salt. EIS tests were performed for each electrolyte composition, see Fig. S1 for a Nyquist plot drawn from the impedance data. In general, the Nyquist plot of an electrolyte should contain two semicircles at high- and mid-frequency regions and a spike at the low frequency region. High and mid frequency semicircles stand for bulk electrolyte and charge transfer resistance at the electrolyte/electrode interface, respectively. The spike at low frequency is due to the capacitive and diffusive features of the electrodes. Each Nyquist plot exhibited the same features as shown in Fig. S1. The absence of high frequency region semicircle might be due to the unavailability of the required high frequency values (equipment limitation). The first interception of the mid frequency semicircle with the real axis of the Nyquist plot gives the bulk electrolyte resistance, R_b which was used to calculate σ [17]. Fig. 2a shows the variation of room temperature conductivity (σ_{RT}) with x. It is seen that the highest σ_{RT} of 7.52×10^{-4} S cm^{-1} was obtained for $x = 0.5$ (weight basis with MG49-NR = 1). This maximum hinders the fact that σ is governed by some factors below and above this x. In general, σ is in relation to three factors as given in Eq. (2)

$$\sigma = ne\mu \tag{2}$$

where $n, e,$ and μ are respectively, the charge carrier concentration, the charge of the electron, and charge carrier mobility [18]. n is low at a low x, and it increases with increasing x. As a result, σ increases with increasing x. However, when a high amount of salt is added to the polymer host, the ions can be close enough to form ion aggregates, which will hinder other free ions' motion (reduce μ) and reduce the density of free mobile ions, thus reducing σ [19]. Whba et al. reported a conductivity value of 1.89×10^{-6} S cm^{-1} for an MG49-NR-based SPE with binary Li salts [20]. Moreover, Priya and Suthanthiraj reported a conductivity value of 5.5×10^{-5} S cm^{-1} for polyvinylidene fluoride co hexafluoropropylene (PVdF-co HFP) based SPE [21]. Compared to these values, our electrolyte is more suitable for practical applications.

XRD analysis is one of the well-known techniques to investigate the crystallinity and amorphous nature of materials. Fig. 2b shows the XRD spectra of MG49-NR polymer, NaTF salt and SPEs with MG49-NR and different ratios of NaTF. The XRD pattern of MG49-NR shows a hump in the region between 10° and 23° corresponding to the amorphous nature of NR and well-defined narrow peaks at 2θ = 29.7°, 36.2°, 39.7°, 43.2°, 47.8°, and 48.8° which is attributed to poly(methyl methacrylate) (PMMA) in the MG49-NR [15,20]. These observations demonstrated the semicrystalline nature of MG49-NR. The XRD spectrum of NaTF shows high intensity diffraction peaks at 2θ = 8.4°, 9.8°, 16.8°, 17.4°, 22.1°, 26.2°, 27.3°, 32.9°, 34.1°, 35.5°, and 40.8° confirming the high

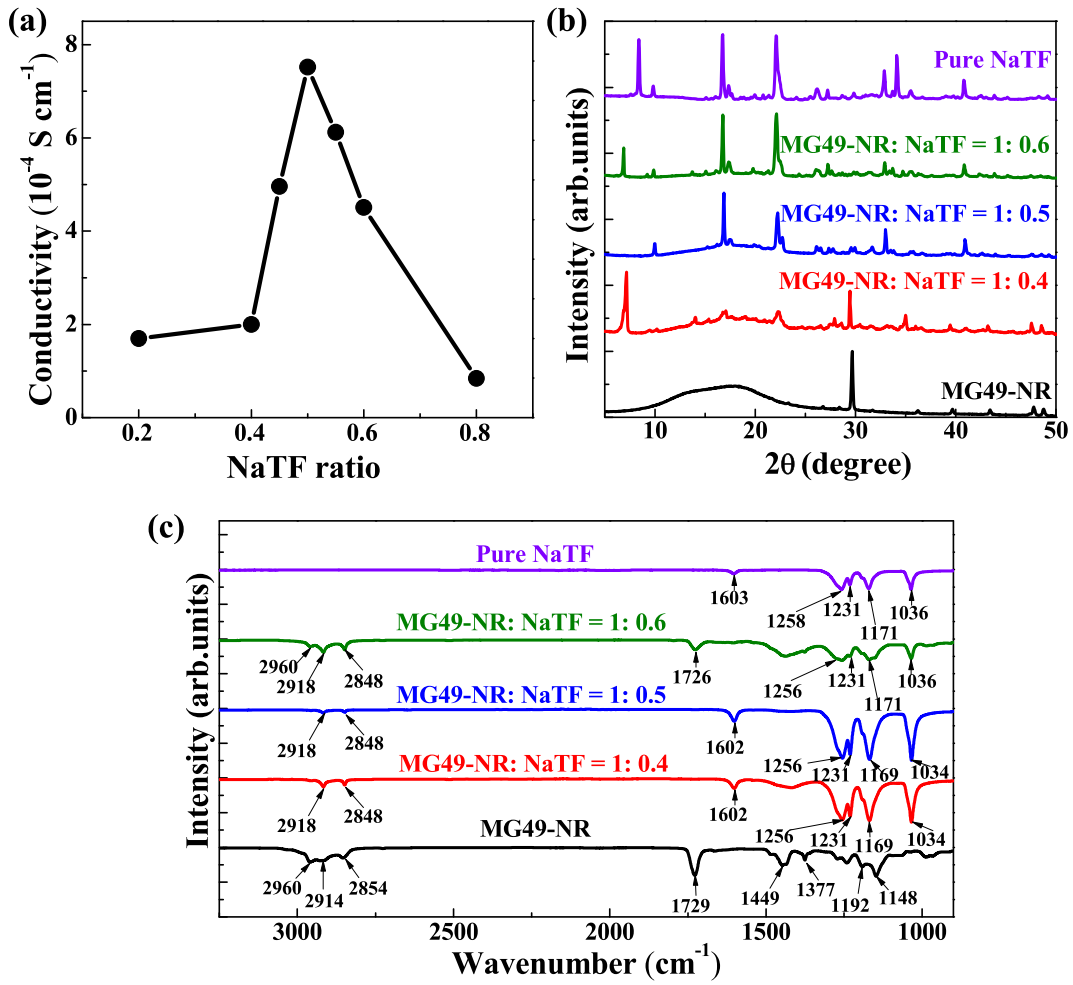

Fig. 2. (a) Dependence of room temperature ionic conductivity on NaTF ratio. (b) XRD and (c) ATR-FTIR spectra of MG49-NR polymer, NaTF salt, and SPEs with MG49-NR and different ratios of NaTF salt.

crystalline nature of the salt. Once the salt is blended with the MG49-NR polymer, the hump in MG49-NR between 10° and 23° reduces with increasing salt ratio. This is due to the reduction of the semicrystalline nature or in other words, the increase of the crystallinity nature of the polymer-salt matrix. When the salt ratio $x > 0.5$, the polymer-salt matrix becomes highly crystalline with many well-defined high intensity peaks corresponding to the NaTF salt.

Table 1 shows the degree of crystallinity for MG49-NR with different ratios of NaTF salt. The degree of crystallinity X_c, is calculated using Eq. (3).

$$X_c = \frac{A_c}{A_c + A_a} \times 100\% \tag{3}$$

where A_c and A_a are respectively, the area of the crystalline peaks and amorphous regions [19]. The degree of crystallinity increases with increasing salt ratio as shown in Table 1. In general, crystalline nature does not support the segmental motion due to the presence of long-range order, thus reducing ionic conductivity. Therefore, conductivity should decrease with increasing salt concentration. However, according to Fig. 2a, conductivity increases with increasing x up to $x = 0.5$. This might be due to the dominant role played by n overriding the crystallinity till x reaches 0.5. For $x > 0.5$, the conductivity decreases may be due to the increase of crystallinity thus reducing the segmental motion and decreasing in μ because of ion aggregation at higher salt concentrations [19].

Table 1
Degree of crystallinity for MG49-NR with different ratios of NaTF.

MG49-NR: NaTF	Crystallinity (%)
1:0	12
1:0.4	46
1:0.5	63
1:0.6	73
0:1	77

The vibrational modes of MG49-NR with different ratios of NaTF were characterized by ATR-FTIR which is a well-established research tool to investigate ion–polymer interaction and possible conformational changes in the host polymer matrix due to the addition of salt. Fig. 2c shows the ATR-FTIR spectra of MG49-NR polymer, NaTF salt, and SPEs with MG49-NR and different ratios of NaTF. Characteristic peaks of MG49-NR polymer and NaTF salt are given in Table 2. In MG49-NR polymer, the main region of interest is the oxygen atoms of the carbonyl group (—C═O) (1740–1700 cm^{-1}) from the PMMA structure in the MG49-NR. The symmetrical stretching of the carbonyl group ν(—C═O) at the wavenumber of 1729 cm^{-1} in PMMA completely disappeared (for $x = 0.4$ and 0.5) or downshifted to 1726 cm^{-1} (for $x = 0.6$) in the polymer-salt matrix. This confirms that the C═O carbonyl group experiences a weak stretching mode due to strong intermolecular interaction [15]. In other words, the bonding length of ν(—C═O) of PMMA becomes longer because the high electronegative value of oxygen atoms pulls the Na^+ ions towards the central atoms, thus stretching the

Table 2
Vibration band assessments of MG49-NR and NaTF salt.

Peak position (cm^{-1})		Vibrational mode
MG49-NR	2960	C—H asymmetric stretching (from methyl) [22]
	2914	C—H asymmetric stretching (from methylene) [22]
	2854	—CH_2- stretching vibration [22]
	1729	C═O [22]
	1449	O—CH_3 [20]
	1377	—CH_3 bending vibration [22]
	1192	C—O [20]
	1148	—C—O—C [22]
NaTF	1603	Characteristic peak of -CF_3SO_3 [23]
	1258	Asymmetric stretching of SO_3 [23]
	1231	Symmetric vibration of CF_3 [20,23]
	1171	—CF_3 asymmetric mode [20,23]
	1036	Symmetric stretching mode of SO_3 [23]

bond between the carbon and oxygen in the carbonyl group.

Changes in the vibrational bands associated with the triflate anion $(CF_3SO_3)^-$ of NaTF salt are investigated to study the interaction between NaTF and MG49-NR. The asymmetric stretching mode of ν_{as}(—SO_3) at 1258 cm^{-1} of NaTF is downshifted to 1256 cm^{-1} in the polymer-salt matrix for all x. However, there were no changes in the peak position of the symmetric stretching mode of ν_s(—CF_3) at 1231 cm^{-1}. On the other hand, the asymmetric stretching of ν_{as}(—CF_3) at 1171 cm^{-1} and the symmetric stretching of ν_s(—SO_3) at 1036 cm^{-1} are downshifted to 1169 cm^{-1} and 1034 cm^{-1}, respectively in the polymer-salt matrix for $x = 0.4$ and 0.5. This weak stretching confirms that the bonding lengths of ν_s(—SO_3) and ν_{as}(—CF_3) become longer due to the changes in the high electronegative value of oxygen atoms that pulled the Na^+ ions towards the —C═O of PMMA in the MG49-NR polymer. However, no changes were observed in the peak positions of the asymmetric stretching of ν_{as}(—CF_3) at 1171 cm^{-1} and the symmetric stretching of ν_s(—SO_3) at 1036 cm^{-1} in the polymer-salt matrix for $x = 0.6$. This shows that the ion aggregation at high salt concentration screening the interaction between the oxygen atoms in the —C═O of PMMA and the Na^+ ions of the NaTF salt. This result supports the observation of a decrease in the room temperature conductivity for $x > 0.5$.

The morphology of the maximum conductivity electrolyte ($x = 0.5$) was studied using SEM and EDX. Fig. 3 shows the SEM images of the electrolyte, confirming well-structured morphology with macroporous due to the interaction between the salt and the polymer host. The average porous size is 28 μm. Fig. 4 shows the backscattered electron image and EDX elemental maps of the electrolyte. The EDX mapping shows the uniform distribution of the NaTF salt across the electrolyte, again confirming that the salt was well mixed with the MG49-NR polymer host. Supporting Information S3 shows the EDX spectrum and the stoichiometric composition of the electrolyte.

3.2. Temperature dependent conductivity study

Understanding the mechanism of ion conduction of an SPE is one of the key attributes to get an insight into its functional limitations. Since conductivity is a temperature dependant parameter, we investigated the variation of conductivity of the optimized SPE (MG49-NR: NaTF = 1:0.5) with temperature. Fig. 5a shows that the conductivity of the SPE increases with increasing temperature. This is due to the increase of ion migration upon their thermal agitation. The linear variation of the natural logarithm of conductivity with inverse temperature suggests that the conductivity mechanism follows the Arrhenius behaviour described by Eq. (4),

$$\sigma = \sigma_0 \, Exp\left(-\frac{E_a}{k_B T}\right) \tag{4}$$

where σ_0 is a proportionality constant, E_a is the activation energy, k_B is the Boltzmann constant and T is the temperature [24]. This observation proposes that ion conduction takes place via the hopping of thermally agitated ions between coordination sites [25]. A similar behaviour has been observed by Priya and Suthanthiraj [21]. The linear fit to the data gives $E_a = 0.29$ eV, which is comparable with the literature values of several other SPEs [26,27].

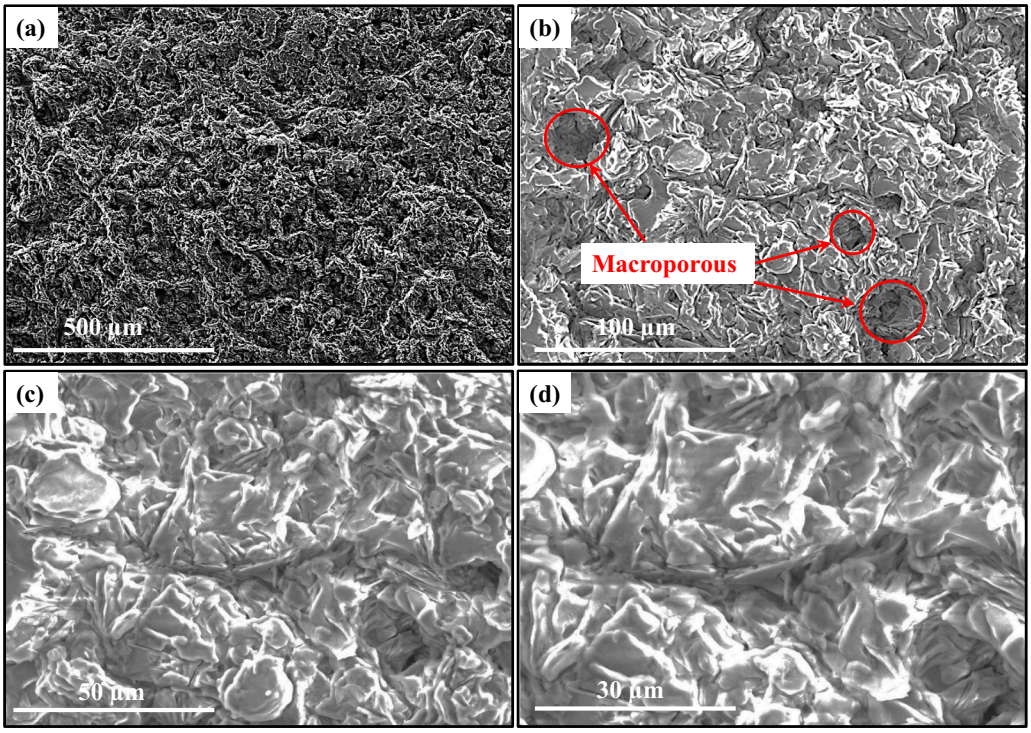

Fig. 3. SEM images of the electrolyte with MG49-NR: NaTF = 1:x at various magnifications. (a) 100×, (b) 500×, (c) 1000×, and (d) 1500×. The images were taken at an acceleration voltage of 10 kV. The red colour circles in (b) indicate macroporous.

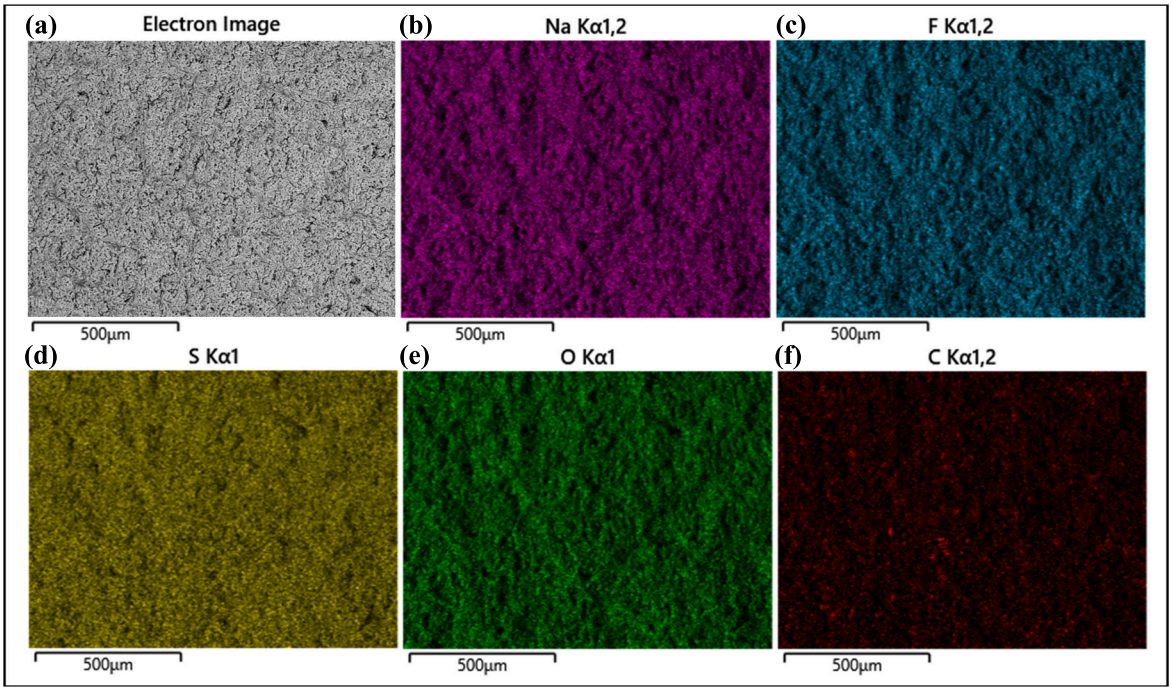

Fig. 4. Backscattered electron image (a) and energy dispersive X-ray (EDX) maps (b–f) of the electrolyte with MG49-NR: NaTF = 1:*x*. The EDX map of elements Na (b), F (c), S (d), O (e), and C (f).

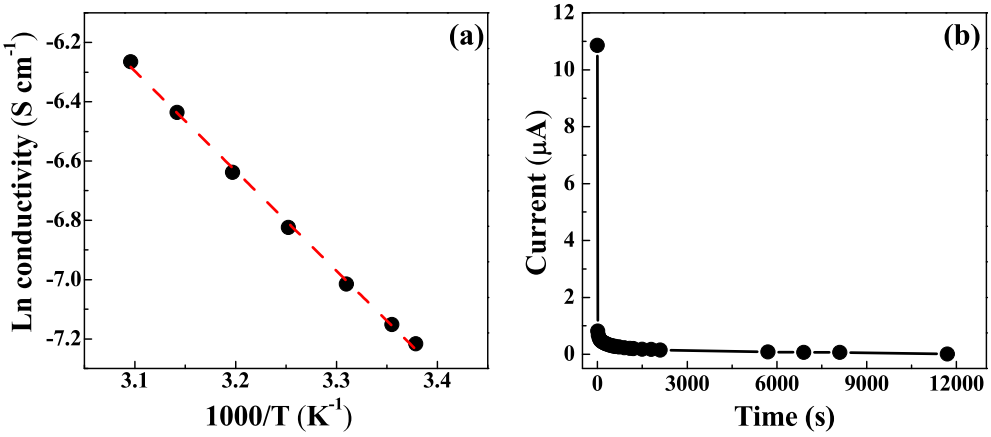

Fig. 5. (a) Dependence of ionic conductivity on the temperature of the optimized electrolyte sample. The dashed line is the linear fit to the data. (b) DC polarization curve obtained under a DC bias potential of 500 mV for the electrolyte sandwiched between two stainless steel (SS) electrodes.

For an electrolyte to be served in any electrochemical device, it should have an appreciable ionic conductivity. Also, its' electronic conductivity should be negligible to avoid short circuits between the electrodes. DC polarization test is a widely used technique to identify the ionic contribution of an electrolyte. In this test, the rate of current flow through the electrolyte sandwiched between two SS electrodes is measured with time to trace the ionic contribution, see Fig. 5b. The ionic transference number t_i is determined using Eq. (5),

$$t_i = \frac{I_t - I_s}{I_t} \tag{5}$$

where I_t and I_s represent the total current and steady-state current, respectively [28]. The resultant value of $t_i = 0.98$, which is close to 1. This confirms that the optimized electrolyte has a dominant ionic contribution to the conductivity.

3.3. Characterization of electrodes

Theoretically, the efficiency and practicality of an electrochemical device primarily depend on the electrode materials. An ideal electrode material would have a high surface area to give many active sites for ion adsorption and desorption. rGO is a suitable electrode material due to its large specific surface area [29,30]. Intifadhah et al. have reported an optimized electrode composition of AC: rGO = 90:10 wt% and polyethylene glycol (PEG) as a binder at a ratio of 1:1 with AC + rGO weight for a sodium sulphate (Na_2SO_4) liquid electrolyte-based double-layer capacitor. They reported a C_{sc} value of 6.26 F g^{-1} [31]. In this current study, we fabricated electrodes with a composition of rGO: AC: PVdF = 80:10:10 wt%. Here PVdF is used as a binder. Fig. 6 shows the BET analysis of the pristine rGO and the rGO composite used for electrodes. After activation under dynamic vacuum at 100 °C, both the pristine rGO and the rGO composite samples exhibit the expected Type IV isotherms with H3 hysteresis behaviour consistent with inter-layer mesoporosity,

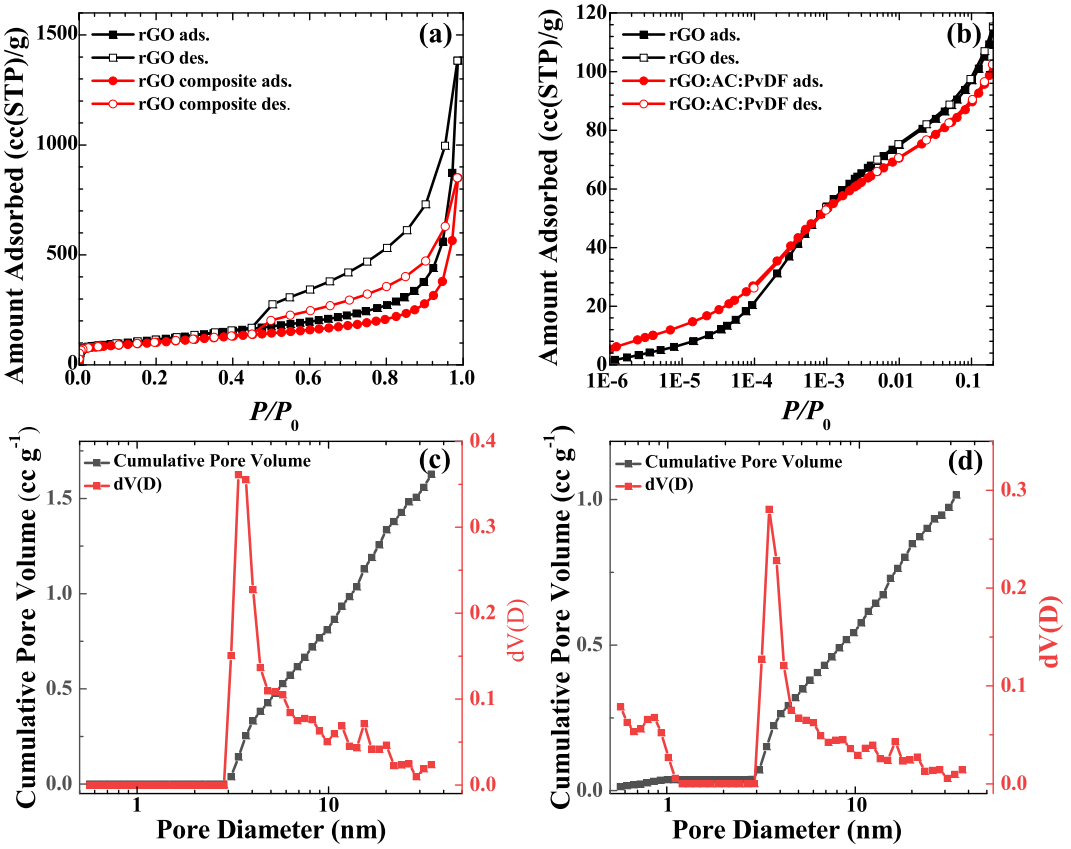

Fig. 6. (a) N_2 adsorption and desorption isotherms at $T = 77$ K for pristine rGO and rGO composite. (b) Expansion of the relative pressure region $1 \times 10^{-6} < P/P_0 < 0.15$ plotted with the logarithmic scale showing the greater adsorption for rGO composite in the micropore region. Calculated pore size distribution plot for (c) pristine rGO, and (d) rGO composite.

as shown in Fig. 6a. The pristine rGO sample exhibited a BET surface area of 411 $m^2\ g^{-1}$. In the rGO composite, the BET surface area lowers slightly to 357 $m^2\ g^{-1}$, a modest decrease likely associated with the mass of the non-porous binder, PVdF. However, as shown in Fig. 6b the rGO composite exhibited higher uptake in the pressure range $P/P_0 < 0.001$, suggesting additional microporosity in this material, likely arising from AC. Based on a QSDFT equilibrium model, the pore size distribution calculation shows the greatest abundance of mesopores with an equivalent 3.4 nm diameter in both materials (see Fig. 6c–d). However, while the pristine rGO contains no significant micropores, the rGO composite exhibits a smaller microporous feature around 0.8 nm contributing 4 % of the combined volume of microporous and mesoporous. The surface morphology of the fabricated electrodes was characterized by SEM imaging. Fig. 7 shows a rough surface with a higher density of interconnected rGO layers. Both BET and SEM analysis confirmed the suitability of the rGO composite electrodes for the charge storage mechanism.

3.4. Characterization of double-layer capacitors

The performance of double-layer capacitors can be evaluated by studying their behaviour concerning different parameters such as frequency, cycling potential window and scan rate. The ultimate goal is monitoring the capability to sustain continuous operation while delivering suitable capacity. The variation of impedance and capacitance dependence on frequency can be sought using EIS. Fig. 8a–b shows a resultant Nyquist plot of a double-layer capacitor which discloses variations of resistive, capacitive features of components of the double-layer

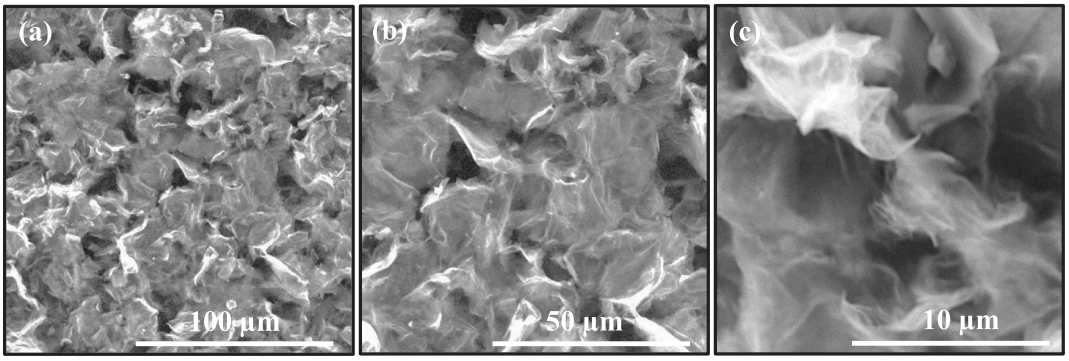

Fig. 7. SEM images of an rGO-based electrode at various magnifications. (a) 500×, (b) 1000×, and (c) 5000×. The images were taken at an acceleration voltage of 10 kV.

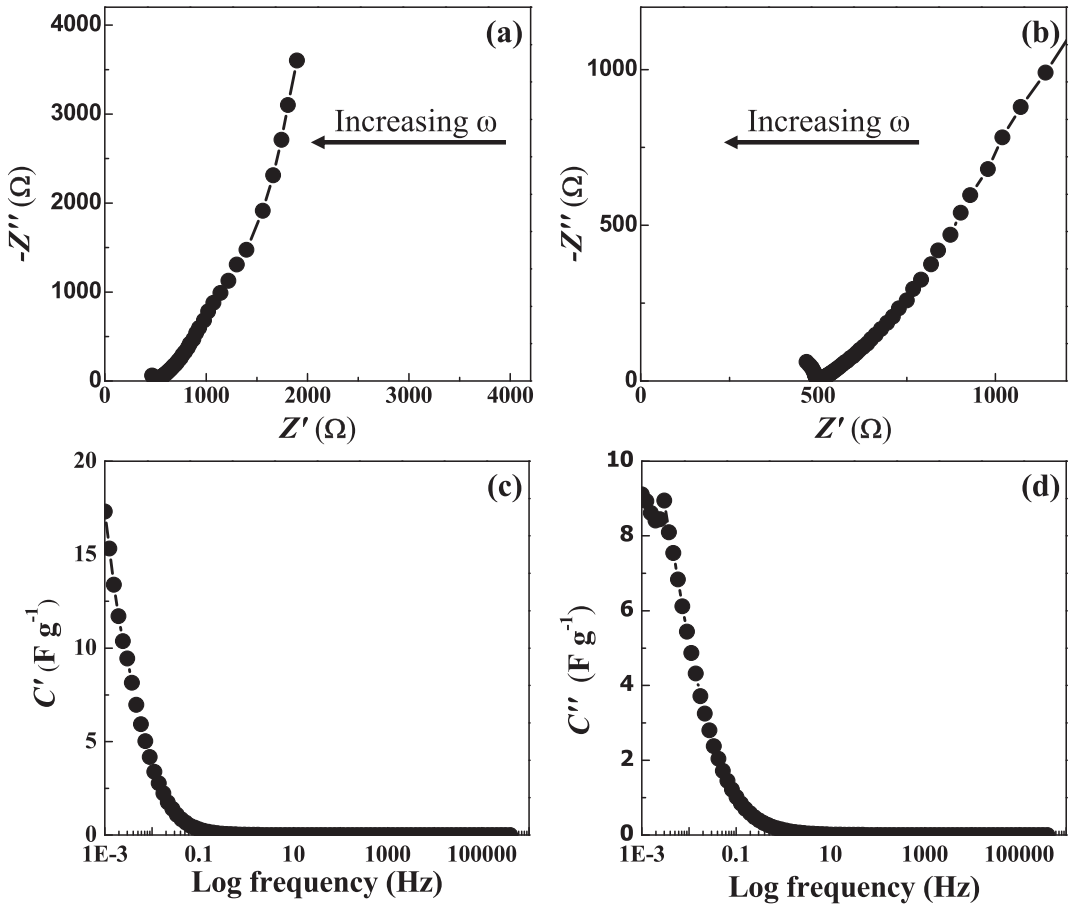

Fig. 8. A Nyquist plot of the double-layer capacitor, rGO-based electrode/MG49-NR-based electrolyte/rGO-based electrode within the frequency range of (a) 0.001 Hz–400 kHZ, and (b) 0.001–1200 Hz at room temperature. Variation of the (c) real and (d) imaginary part of capacitance with frequency.

capacitor with respect to frequency. The bulk electrolyte and charge transfer resistances can be observed as semicircles at high and mid frequencies. However, no semicircles were seen in this investigation which may be due to the unavailability of the high frequency range (equipment limitation). Fig. 8b is an expanded version of the high and mid-frequency regions of Fig. 8a. The total resistance of the electrolyte and electrode is around 500 Ω. The two spikes at the low frequency region represent the Warburg diffusion and capacitive features. The near parallel spike with the imaginary impedance axis stands for the capacitive nature of the double-layer capacitor.

The dependence of complex capacitance on frequency (f) can be obtained by plotting real $C'(\omega)$ and imaginary $C''(\omega)$ capacitive components with log frequency as the Bode plot shown in Fig. 8c–d. Real and imaginary capacitive values were calculated using the impedance data described by Eqs. (6) and (7).

$$C' = -Z''/\omega\,|Z(\omega)\,| \tag{6}$$

$$C'' = Z'/\omega\,|Z(\omega)\,| \tag{7}$$

where, $Z(\omega)$ is the complex impedance, ω is the angular frequency ($\omega = 2\pi f$), Z' is the real part of complex impedance, and Z'' is the imaginary part of complex impedance [17]. The capacitive features become dominant at low frequencies, whereas the resistive features override the capacitive features at high frequencies. Therefore, the capacitance decreases drastically with increasing frequency as seen in Fig. 8c. At high frequencies, the device becomes a pure resistor. The maximum value on the real capacitive axis relates to the single electrode C_{sc} value. It is 17.1 F g^{-1} for the fabricated double-layer capacitor. Fig. 8d shows the dependence of the imaginary part of capacitance with frequency. The maximum position of the curve represents the complete system, which describes the transition point at which the device changes its behaviour from purely capacitive to purely resistive character [5]. In other words, the peak frequency (f_0) is characterized as the position of equal resistive and capacitive impedance. The relaxation time constant (τ_0) is defined as the minimum time for discharging all energy from a device that has an efficiency >50 % [17]. Therefore, τ_0 can be described as Eq. (8),

$$\tau_0 = {}^{1}/_{2\pi f_0} \tag{8}$$

Our fabricated double-layer capacitor shows f_0 = 3.01 mHz, thus giving τ_0 = 52.85 s. This value is quite high compared to reported values for different supercapacitor configurations [32]. This hints that the ion transfer process that is responsible for discharging should be somewhat slower in the fabricated double-layer capacitor. It means that the ion movement may be hindered within the rGO composite electrode or across the electrode/electrolyte interface, even though the electrolyte has a substantial ionic conductivity [13]. Some possible reasons might be narrow ion conduction paths in the electrodes and a large gap between the electrode and the electrolyte [15].

In the CV test, current is measured across the capacitor by varying the potential window and cycling at a specific scan rate. Fig. 9a illustrates the cyclic voltammograms obtained for the double-layer capacitor by cycling in different potential windows at a scan rate of 10 mV s^{-1}. All cyclic voltammograms showed an almost parallelogram shape which is relevant to double-layer capacitive features [33]. However, an increase in current while widening the potential window from 0.8 V to 1.6 V slightly destroyed the symmetry around the potential axis. This might be due to the onset of any unwanted reactions at high potentials that destroy the electrolyte and/or electrode. Considering this fact, the

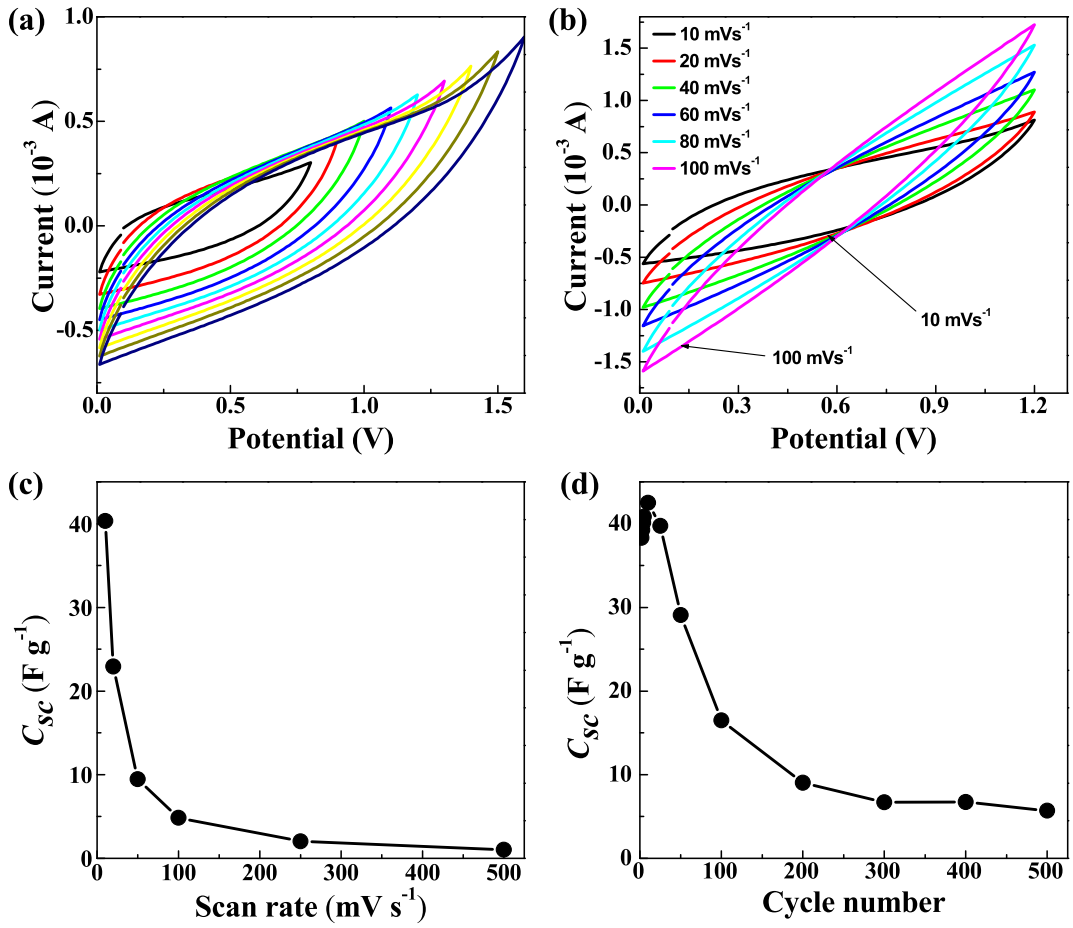

Fig. 9. (a) Cyclic voltammograms in different potential windows at a scan rate of 10 mV s^{-1}. (b) Resulted cyclic voltammograms with variation in scan rates. (c) Variation of the single electrode specific capacitance (C_{sc}) with scan rate. (d) Variation of the single electrode specific capacitance (C_{sc}) with cycle number at a scan rate of 10 mV s^{-1}.

potential window up to 1.2 V was selected for further studies. All cyclic voltammograms do not have peaks which verify the absence of redox reactions. Peaks appear at the potentials where redox reactions take place. Fig. 9b shows the cyclic voltammograms resulting from variations in scan rates. All cyclic voltammograms do not have any peak again symbolising the absence of redox reactions. As the scan rate increases, it is seen that the current is delayed in reaching a constant value upon reversing the potential scan. This is mainly due to equivalent series resistance as reported by Arof et al. [34].

Scan rate is an important parameter to determine the occurrence of complete reactions that are responsible for the charge storage mechanism. There is ample time for the reactions to take place completely at low scan rates. In other words, electrolyte ions diffuse well towards the external surface and inner active sites of electrodes leading to higher capacitance at low scan rates [35]. However, there is not enough time for complete reactions at high scan rates, which leads to poor charge storage. This is clearly seen in Fig. 9c which illustrates the variation of the C_{sc} with the scan rate. C_{sc} was calculated using Eq. (9)

$$C_{sc} = 2\int IdV \Big/ mS\triangle V \tag{9}$$

where $\int IdV$ is the area of a cyclic voltammogram, m is the mass of an electrode, S is the scan rate and $\triangle V$ is the potential window [32]. Here the factor "2" is due to the assumption that the double-layer capacitor contains two identical capacitors corresponding to each electrode connected in series. The value of C_{sc} decreases with increasing scan rate as explained before. A similar observation was reported by many research groups [36,37]. However, very low scan rates are also not favourable since there is a possibility of parasitic reactions occurring other than the usual non-faradic reactions needed for the charge storage mechanism. Therefore, a scan rate of 10 mV s^{-1} was chosen as a suitable value for continuous cyclic study.

Continuous performance of a device is one of the key parameters that determine the suitability for real world applications. Fig. 9d shows the variation of C_{sc} with cycle number. Soon after the fabrication of the double-layer capacitor, the contacts between the electrodes and the electrolyte may not have formed very well. These contacts could become more stable after several initial cycles. Thus, C_{sc} increases during initial cycles and reaches a maximum value of 42.5 F g^{-1} within the first 25 cycles. Afterwards, the C_{sc} value decreases with increasing cycle number. This might be due to the degradation of the electrolyte and/or electrodes or changes at the interfaces. Moreover, there might be some irreversible reactions like charge trapping leading to the fade of C_{sc}.

The ability to withstand continuous charge discharge operation under a constant current and within two specific potential limits is another important feature of any electrochemical device. Supporting Information S5 shows the GCD measurement. Fig. 10 illustrates the variation of single electrode specific discharge capacitance (C_{sd}) of the double-layer capacitor with continuous cycling at a current density of 0.05 A g^{-1}. The initial C_{sd} value of 15.5 F g^{-1} reduced to 0.81 F g^{-1} during 10,000 cycles. A steep reduction has existed during the first 1000 cycles (see Fig. 10a). This might be due to some irreversible structural changes of the electrodes that take place at the initial cycles. Yadav et al. reported another possible reason for this as a blockage of a few small-sized pores/micropores while insertion/de-insertion of electrolyte ions

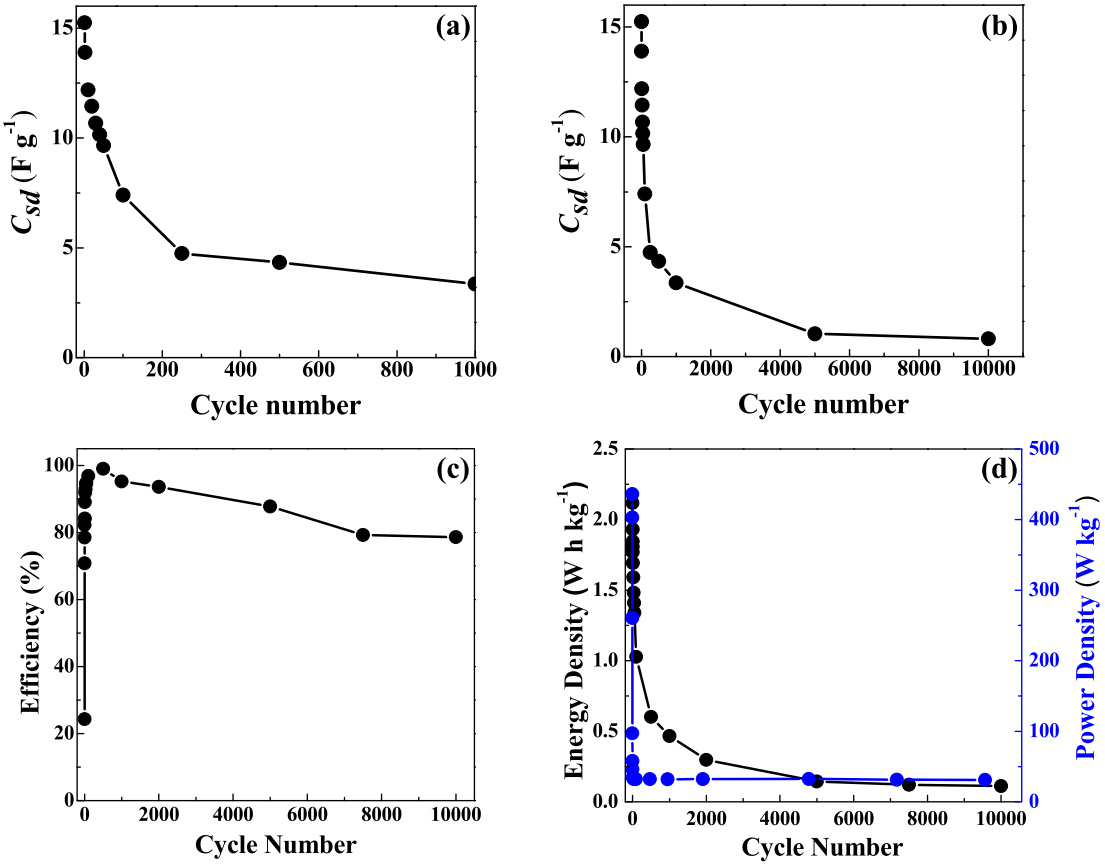

Fig. 10. Variation of single electrode specific discharge capacitance, C_{sd} with continuous (a) 1000 and (b) 10,000 cycling at a constant current density of 0.05 A g^{-1} within the potential window of 0.2–1.2 V. Dependence of (c) efficiency, and (d) energy and power densities on cycle number.

during the initial charge-discharge process [38]. However, the rate of reduction becomes smaller after 5000 cycles (see Fig. 10b) which may be due to no major structural changes in the electrodes or at the interfaces between the electrode and electrolyte. This is an encouraging observation to improve the electrode properties towards further development.

The dependence of efficiency on number of cycles is shown in Fig. 10c. Efficiency has increased from 24 % to 99 % within the first 500 cycles. Thereafter, it started to drop and saturated at a value of around 79 % after 7500 cycles. Lower efficiency is expected at the initial cycles due to the immaturity of the device. However, due to ageing and possible degradation reactions, efficiency can significantly drop. During continuous operation, ion pathways may become tortuous due to the presence of micropores in the rGO composite electrodes thus disturbing the charge storage. As a result, efficiency could be reduced. Fig. 10d shows the dependence of energy density (E) and power density (P) on number of cycles. The energy and power densities were calculated using Eqs. (10) and (11).

$$E\ (\mathrm{W\ h\ kg^{-1}}) = (1/2)C_{sd}\ V^2 \times 1000/3600 \tag{10}$$

$$P\ (\mathrm{W\ kg^{-1}}) = E \times 3600/t \tag{11}$$

where, V is the voltage (V), and t is the discharge time (s) [39]. The first cycle shows an E of 2.11 W h kg^{-1} whereas it reduces to 0.11 W h kg^{-1} at the 10000th cycle. According to the Ragone plot, E values of supercapacitors should lie between 0.05 and 20 W h kg^{-1} [39]. The fabricated double-layer capacitor possesses that energy range of up to >10,000 cycles, which is a promising result. On the other hand, the decrease of P from 436 W kg^{-1} to 32 W kg^{-1} within the first 50 cycles could be attributed to the interfacial issues between the electrode and electrolyte. Even though the value of P drastically drops at the beginning, it saturated after the 50th cycle around 32 W kg^{-1} which falls within the range of 9 – 10000 W kg^{-1} stipulated by the Ragone plot [39].

Table 3 shows the comparison of our results with the literature. The results of our current study are comparable with the reported values for the electrochemical double layer capacitors which contain MG-NR-based electrolytes [12–15]. However, the performance of our double-layer capacitor can be optimized by further improving the properties of the electrolyte, electrode, and the electrode/electrolyte interface. Incorporating an ionic liquid or redox additive could improve the ionic conductivity of the electrolyte [10,23,24]. Further optimization of the electrode can be done by annealing the rGO under Ar + H_2 environment for a temperature above 400 °C to remove any contaminations and water absorption from the ambient environment. Moreover, ball milling could improve its structural properties.

4. Conclusion

In this study, SPEs containing MG49-NR and different ratios of NaTF salt were fabricated and characterized by impedance measurement, XRD and ATR-FTIR spectroscopy. The composition MG49-NR: NaTF = 1:0.5 (weight basis) showed the highest σ_{RT} of 7.52 × 10^{-4} S cm^{-1}. This optimized electrolyte sample is predominantly an ionic conductor with E_a = 0.29 eV. Double-layer capacitors were assembled by sandwiching the optimized electrolyte between two identical rGO-based electrodes and characterized by EIS, CV and GCD tests. EIS measurements showed that capacitive features override the resistive features at low frequencies. A maximum C_{sc} value of 42.5 F g^{-1} was obtained via the CV test at the scan rate of 10 mV s^{-1} within the potential window of 0.8 V to 1.2 V. Under the GCD test, continuous charging and discharging cycling was performed for 10,000 cycles at a constant current density of 0.05 A

Table 3
Comparison of different SPEs and electrodes for supercapacitor performance.

Electrolyte		Room temperature conductivity (S cm^{-1})	Electrode	Single electrode specific capacitance (max) (F g^{-1})	Energy density (max) (W h kg^{-1})	Power density (max) (W kg^{-1})	Reference
Polymer	Salt and/or ionic liquid						
PEO + ENR-50	LiTFSI	6.45×10^{-5}	–	–	–	–	[9]
MG30-NR- 6PPD + TMG30 additive	LiTF	1.5×10^{-2}	–	–	–	–	[10]
MG49-NR	$LiClO_4$	3.5×10^{-5}	–	–	–	–	[11]
MG30-NR	$LiClO_4$	6.2×10^{-7}	–				[11]
MG49-NR	$LiBF_4$ + LiI	1.89×10^{-6}	–	–	–	–	[20]
PVdF-HFP	ZnTF	5.5×10^{-5}	–	–	–	–	[21]
PVdF-HFP	NaTF + PMII	1.37×10^{-3}	–	–	–	–	[23]
PVP/PVdF-HFP	[bdmim]BF4	2.92×10^{-3}	Porous carbon	117	14	21	[24]
MG30-NR	$NH_4CF_3SO_3$ + ethylene carbonate (EC)	9.61×10^{-4}	AC	32	–	–	[12]
MG49-NR	ZnTF	0.6×10^{-4}	Natural graphite (NG)	2.26	–	–	[13]
NR	LiTFSI	–	NG + PVdF	4.8	–	–	[14]
MG49-NR	ZnTF	0.6×10^{-4}	NG + AC + PVdF	30.85	1.69	46.9	[15]
MG49-NR	NaTF	7.52×10^{-4}	rGO + AC + PVdF	42.5	2.11	436	Present study

g^{-1} within the potential window of 0.2 V to 1.2 V. Even though the C_{sd} value dropped fast at the beginning, it started to saturate after the 5000th cycle proving the good stability of the capacitor. This study proves the suitability of MG49-NR + Na salt-based electrolyte and rGO-based electrodes for supercapacitor performance. Further improvements can be made by improving the structural properties of the rGO-based electrodes and electrode/electrolyte interface.

CRediT authorship contribution statement

Kumudu S. Perera: Writing – original draft, Methodology, Investigation, Formal analysis, Data curation, Conceptualization. **Kamal P. Vidanapathirana:** Writing – review & editing, Methodology, Investigation, Formal analysis, Data curation, Conceptualization. **Lewis J. Adams:** Data curation. **Chris S. Hawes:** Data curation. **Nilanthy Balakrishnan:** Writing – original draft, Supervision, Resources, Funding acquisition, Formal analysis, Conceptualization.

Declaration of competing interest

The authors declare the following financial interests/personal relationships which may be considered as potential competing interests:

Nilanthy Balakrishnan reports financial support was provided by Engineering and Physical Sciences Research Council. Lewis J Adams reports financial support was provided by Keele University. Kumudu S. Pereraa, Kamal P. Vidanapathirana reports financial support was provided by Wayamba University of Sri Lanka. If there are other authors, they declare that they have no known competing financial interests or personal relationships that could have appeared to influence the work reported in this paper.

Data availability

The data that support the findings of this study are openly available in the Keele Data Repository at https://doi.org/10.21252/j0g1-8b10.

Acknowledgements

This work was supported by the Engineering and Physical Sciences Research Council (EPSRC) [under grant EP/Y003462/1], Keele University, and Wayamba University of Sri Lanka. The authors acknowledge Associated Speciality Rubbers (PVT) Ltd., Sri Lanka and Sakura Graphite, Ragedara Mine, Sri Lanka for providing MG49-NR and rGO samples, respectively.

Appendix A Supplementary data

BET surface area analysis of pristine rGO and rGO composite, Nyquist plot of the high conductivity electrolyte, EDX analysis of the high conductivity electrolyte, optical images of the MG49-NR + NaTF electrolyte, rGO composite electrode, and the symmetric double-layer capacitor, and GCD measurement of the fabricated double-layer capacitor. Supplementary data to this article can be found online at https://doi.org/10.1016/j.est.2024.112683.

References

[1] P. Bradu, A. Biswas, C. Nair, S. Sreevalsakumar, M. Patil, S. Kannampuzha, A. G. Mukherjee, U.R. Wanjari, K. Renu, B. Vellingiri, A.V. Gopalakrishnan, Recent advances in green technology and industrial revolution 4.0 for a sustainable future, Environ. Sci. Pollut. Res. 30 (2023) 124488–124519.
[2] V. Aravindan, J. Gnanaraj, Y.S. Lee, S. Madhavi, Insertion-type electrodes for nonaqueous Li-ion capacitors, Chem. Rev. 114 (2014) 11619–11635.
[3] D.E. Fenton, J.M. Parker, P.V. Wright, Com-plexes of alkali metal ions with poly (ethylene oxide), Polymer 14 (1973) 589.
[4] N. Kumar, M. Sahu, D.K. Sahu, Y.K. Mahipal, Investigation of ZnO nano-filler-dispersed nano-composite polymer electrolytes and their ion transport property, J. Solid State Electrochem. 26 (2022) 1613–1626.
[5] A. Jain, S.K. Tripathi, A. Gupta, M. Kumari, Fabrication and characterization of electrochemical double-layer capacitors using ionic liquid-based gel polymer electrolyte with chemically treated activated charcoal electrodes, J. Solid State Electrochem. 17 (2013) 713–726.
[6] R. Idris, M.D. Glasse, R.J. Latham, R.G. Linford, W.S. Schlindwein, Polymer electrolytes based on modified natural rubber for use in rechargeable lithium batteries, J. Power Sources 94 (2001) 201–206.
[7] A. Ahmad, M.Y.A. Rahman, H. Harun, M.S. Su'ait, M.A. Yarmo, Preparation and characterization of 49% poly(methyl methacrylate) grafted natural rubber (MG49)-stannum (IV) oxide (SnO_2)-lithium salt based composite polymer electrolyte, Int. J. Electrochem. Sci. 7 (2012) 8309–8325.
[8] S.A.M. Noor, A. Ahmad, I.A. Talib, M.Y.A. Rahman, Effect of ZnO nanoparticles filler concentration on the properties of PEO-ENR50-$LiCF_3SO_3$ solid polymeric electrolyte, Ionics 17 (2011) 451–456.
[9] T.K. Lee, N.F.M. Zaini, N.N. Mobara, N.H. Hassan, S.A.M. Noor, S. Mamat, K.S. Loh, K.H. KuBulat, M.S. Su'ait, A. Ahmad, PEO based polymer electrolyte comprised of epoxidized natural rubber material (ENR50) for Li-ion polymer battery application, Electrochim. Acta 316 (2019) 283–291.
[10] A.F. Aziz, K. Nazir, S.F. Ayub, N.I. Adam, M.Z.A. Yahya, A.M.M. Ali, Electrochemical properties of polymer electrolytes treated with 6PPD on 30% poly (methyl methacrylate) grafted natural rubber, Malaysian J. Analytical Sci. 22 (3) (2018) 491–498.

[11] S.N.H.M. Yusoff, L.H. Sim, C.H. Chan, S.S.S.A. Aziz, Z.S. Mahmud, H.M. Hairi, Studies on thermal and conductivity of modified natural rubber, J. Adv. Res. Mater. Sci. 12 (1) (2015) 1–11. ISSN (online): 2289–7992.
[12] N.H.M. Zaki, Z.S. Mahmud, O.H. Hassan, M.Z.A. Yahya, A.M.M. Ali, A symmetric supercapacitor based on 30% poly (methyl methacrylate) grafted natural rubber (MG30) polymer and activated carbon electrodes, AIP Conf. Proc. 1875 (2017) 020016, https://doi.org/10.1063/1.4998370.
[13] N. Rajapaksha, K.S. Perera, K.P. Vidanapathirana, Analysis of electrochemical double-layer capacitors using a natural rubber-Zn based polymer electrolyte, Adv. Energy Res. 8 (1) (2022) 41–57.
[14] N.A.A.K. Sanjaya, K.P. Vidanapathirana, K.S. Perera, A natural rubber based electrolyte to be used in EDLCs with Sri Lankan graphite, Mater. Today Proc. 23 (1) (2020) 30–33.
[15] K.S. Perera, K.P. Vidanapathirana, L.J. Adams, N. Balakrishnan, Sustainable supercapacitors with a natural rubber-based electrolyte and natural graphite-based electrodes, Electrochem. Sci. Adv. (2023) e2300025, https://doi.org/10.1002/elsa.202300025.
[16] T.S. Tiong, M.H. Buraidah, L.P. Teo, A.K. Arof, Conductivity studies of polyethylene oxide/polyvinylialcohol blend gel polymer electrolytes for dye sensitized solar cells, Ionics 22 (2016) 2133–2142.
[17] N.O. Laschuk, E.B. Easton, O.V. Zenkina, Reducing the resistance for the use of electrochemical impedance spectroscopy analysis in materials chemistry, RSC Adv. 11 (2021) 27925–27936.
[18] C. Liang, B. Jabar, C. Liu, Y. Chen, Z. Zheng, P. Fan, Fu Li, Optimized thermoelectric properties of sulfide compound Bi_2SeS_2 by iodine doping, Nanomaterials 12 (2022) 2434–2445.
[19] S.B. Aziz, O.G. Abdullah, M.A. Rasheed, H.M. Ahmed, Effect of high salt concentration (HSC) on structural, morphological, and electrical characteristics of chitosan based solid polymer electrolytes, Polymers 9 (2017) 187.
[20] R.A.G. Whba, L. TianKhoon, M.S. Su'ait, M.Y.A. Rahman, A. Ahmad, Influence of binary lithium salts on 49% poly (methyl methacrylate) grafted natural rubber based solid polymer electrolytes, Arab. J. Chem. 13 (2020) 3351–3361.
[21] W.L.M. Priya, A. Suthanthiraj, Preparation and characterization of electrolytes containing polyvinylidene fluoride co hexafluoropropylene and zinc trifluoromethanesulfonate, Chem. Sci. Trans. 2 (4) (2013) 1232–1237.
[22] J. Coates, Interpretation of infrared spectra, a practical approach, in: R.A. Meyers (Ed.), Encyclopedia of Analytical Chemistry, John Wiley & Sons Ltd, Chichester, 2000, pp. 10815–10837.
[23] S. Jeya, A. Arulsankar, S. Abarna, B. Sundaresan, Effect of ionic liquids on the electrical, structural and morphological properties of P(VdF-HFP)–NaTF electrolytes, Ionics 25 (2019) 5963–5977.
[24] S.N. Syahidah, S.R. Majid, Ionic liquid based gel electrolytes for symmetrical solid state electrical double layer capacitor operated at different operating voltages, Electrochim. Acta 175 (2015) 184–192.
[25] R.M.L.L. Rathnayake, K.S. Perera, K.P. Vidanapathirana, Past, present and future of ionic liquid based polymer electrolytes, AIMS Energy. 8 (2020) 231.
[26] M.F.Z. Kadir, S.R. Majid, A.K. Arof, Plasticized chitosan–PVA blend polymer electrolyte based proton battery, Electrochim. Acta 55 (2010) 1475–1482.
[27] L.S. Ng, A.A. Mohamad, Effect of temperature on the performance of proton batteries based on chitosan–NH_4NO_3–EC membrane, J. Membr. Sci. 325 (2008) 653.
[28] S.B. Aziz, R.T. Abdulwahid, M.H. Hamsan, M.A. Brza, R.M. Abdullah, M.F.Z. Kadir, S.K. Muzakir, Structural, impedance, and EDLC characteristics of proton conducting chitosan-based polymer blend electrolytes with high electrochemical stability, Molecules 24 (2019) 3508–3523.
[29] A.T. Smith, A.M. LaChance, S. Zeng, B. Liu, L. Sun, Synthesis, properties, and applications of graphene oxide/reduced graphene oxide and their nanocomposites, Nano Mater. Sci. 1 (2019) 31–47.
[30] G. Folaranmi, M. Bechelany, P. Sistat, M. Cretin, F. Zavisk, Activated carbon blended with reduced graphene oxide nanoflakes for capacitive deionization, Nanomaterials 11 (2021) 1090.
[31] S.H. Intifadhah, L. Rohmawati, W. Setyarsih, Tukiran, The effect of rGO mass composition on the performance of activated carbon/rGO supercapacitor electrode based on coconut shell (Cocos nucifera), J. Phys. Conf. Ser. 1108 (2018) 012045.
[32] J.P. Tey, M.A. Careem, M.A. Yarmo, A.K. Arof, Durian shell-based activated carbon electrode for EDLCs, Ionics 22 (2016) 1209–1216.
[33] X. You, M. Misra, S. Gregori, A.K. Mohanty, Preparation of an electric double layer capacitor (EDLC) using miscanthus-derived biocarbon, ACS Sustain. Chem. Eng. 6 (2018) 318.
[34] A.K. Arof, M.Z. Kufian, M.F. Syukur, M.F. Aziz, A.E. Abdelrahman, S.R. Majid, Electrical double layer capacitor using poly(methyl methacrylate)–C_4BO_8Li gel polymer electrolyte and carbonaceous material from shells of *mata kucing* (*Dimocarpus longan*) fruit, Electrochim. Acta 74 (2012) 39–45.
[35] Y. Xie, H. Du, Electrochemical capacitance of a carbon quantum dots–polypyrrole/titania nanotube hybrid, RSC Adv. 5 (2015) 89689.
[36] P.F.R. Ortega, J.P.C. Trigueiro, G.G. Silva, R.L. Lavall, Nanocomposites of graphene nanosheets/multiwalled carbon nanotubes as electrodes for in-plane supercapacitors, Electrochim. Acta 188 (2016) 809–817.
[37] J.S. Shayeha, A. Ehsani, M.R. Ganjali, P. Norouzi, B. Jaleh, Conductive polymer/reduced graphene oxide/Au nano particles as efficient composite materials in electrochemical supercapacitors, Appl. Surf. Sci. 353 (2015) 594–599.
[38] N. Yadav, S.A. Hashmi, Energy enhancement of quasi-solid-state supercapacitors based on a non-aqueous gel polymer electrolyte via a synergistic effect of dual redox additives diphenylamine and potassium iodide, J. Mater. Chem. A 35 (2020) 18266–18279.
[39] S.K. Poonam, A. Arora, S.K. Tripathi, Review of supercapacitors: materials and devices, J. Energy Storage. 21 (2019) 801–825.